Atherosclerosis 420 (2026) 121857

Contents lists available at ScienceDirect

Atherosclerosis

journal homepage: www.elsevier.com/locate/atherosclerosis

Deficiency of the aryl hydrocarbon receptor in intestinal epithelial cells, but not hepatocytes, ameliorates atherosclerosis development by sex-dependently targeting the lipid metabolism

Rosanna Huchzermeier[a,b,c], Leonida Rakateli[a,b], Melissa Corcini-Berndt[a,b,c], Sanne L. Maas[a,b,c], Kathrin Abschlag[a,b,c], Chantal Maassen Pöttgens[a,b,c], Julia Moellmann[a], Tabea Pirker[a], Susanne Kremer[d], Julia Steitz[d], Han Jin[e,f], Boyu Ji[g], Stefan Düsterhöft[h], Caspar Ohnmacht[i], Renske J. de Jong[j], Emiel P.C. van der Vorst[a,b,c,k,*]

[a] Department of Internal Medicine I, University Hospital Aachen, RWTH Aachen University, Aachen, Germany
[b] Institute for Molecular Cardiovascular Research (IMCAR), Uniklinik RWTH Aachen, RWTH Aachen University, Aachen, Germany
[c] Aachen-Maastricht Institute for Cardio-Renal Disease (AMICARE), Uniklinik RWTH Aachen, RWTH Aachen University, Aachen, Germany
[d] Institute for Laboratory Animal Science, Medical Faculty, RWTH Aachen University, Aachen, Germany
[e] Central Laboratory, Tianjin Medical University General Hospital, Tianjin, China
[f] Department of Pathology, Cardiovascular Research Institute Maastricht (CARIM), Maastricht University Medical Center+, Maastricht, the Netherlands
[g] Tianjin Institute of Immunology, Department of Immunology, Tianjin Key Laboratory of Cellular and Molecular Immunology, Key Laboratory of Diseases and Microenvironment of Ministry of Education of China, Tianjin Medical University, Tianjin, China
[h] Institute of Molecular Pharmacology, Medical Faculty, RWTH Aachen University, Aachen, Germany
[i] Center of Allergy and Environment (ZAUM), Technical University and Helmholtz Center Munich, Munich, Germany
[j] Department of Pediatrics, RWTH Aachen University, Aachen, Germany
[k] Institute for Cardiovascular Prevention (IPEK), Ludwig-Maximilians-Universität, Munich, Germany

HIGHLIGHTS

- AhR is identified as a key regulator of intestinal lipid metabolism in males.
- Intestinal epithelial-cell *Ahr* deficiency reduces atherosclerosis.
- No clear phenotype in hepatocyte *Ahr*-deficient mice under the present experimental conditions.

GRAPHICAL ABSTRACT

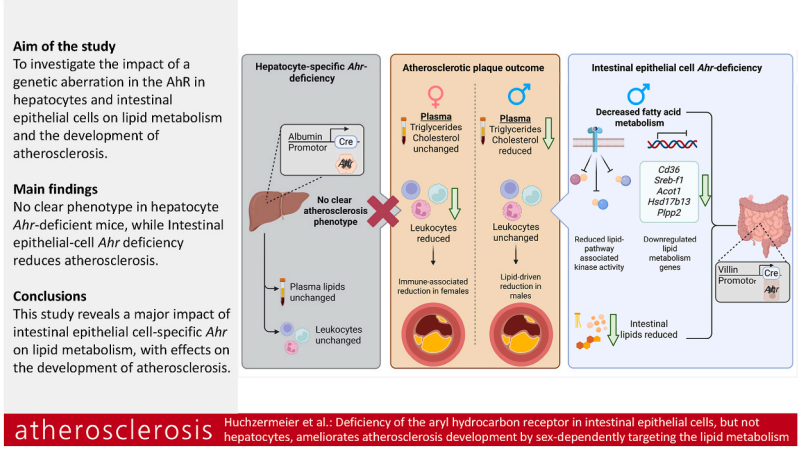

* Corresponding author. Department of Internal Medicine I, University Hospital Aachen, RWTH Aachen University, Aachen, Germany.
E-mail address: evandervorst@ukaachen.de (E.P.C. van der Vorst).

https://doi.org/10.1016/j.atherosclerosis.2026.121857
Received 13 February 2026; Received in revised form 20 July 2026; Accepted 21 July 2026
Available online 26 July 2026

ARTICLE INFO

Keywords:
Aryl hydrocarbon receptor
Intestinal lipid metabolism
Atherosclerosis
Sex dimorphism

ABSTRACT

Background: The aryl hydrocarbon receptor (AhR) is a well-described regulator of xenobiotic stimuli, but recent studies highlight a potential bidirectional role in mediating lipid metabolism. The precise mechanisms underlying these effects are not yet fully understood. Therefore, this study aimed to investigate the impact of a genetic aberration in the AhR in hepatocytes and intestinal epithelial cells on lipid metabolism and the development of atherosclerosis.

Methods: By injecting Albumin-iCre containing AAVs into PCSK9 overexpressing $Ahr^{fl/fl}$ mice, hepatocyte-specific *Ahr*-deficient mice were created. Additionally, mice with an intestinal epithelial cell-specific deficiency of the *Ahr* ($Ahr^{fl/fl}$ $Villin^{Cre+}$) and control mice ($Ahr^{fl/fl}$) were injected with AAV8-PCSK9. Both mouse models were fed a high-fat diet (HFD) for 12 weeks, after which alterations in plasma lipid levels and the development of atherosclerosis were assessed.

Findings: Mice lacking hepatocyte-specific *Ahr* did not exhibit significant differences in lipid levels or atherosclerosis. In contrast, male mice lacking *Ahr* in intestinal epithelial cells (IECs) showed significant changes in intestinal and systemic lipid levels, which coincided with altered RNA transcription and intestinal kinase activity, whereas female mice were unaffected. Interestingly, female mice showed reduced circulating leukocyte counts, whereas males were unaffected. Combined, these alterations resulted in decreased atherosclerosis development in both sexes.

Interpretation: This study reveals a major impact of intestinal epithelial cell-specific *Ahr* on lipid metabolism, with effects on atherosclerosis development, particularly in male mice, whereas atherosclerosis development in female intestinal epithelial cell-specific *Ahr*-deficient mice is accompanied by reduced circulating leukocytes, thereby suggesting apparent sex dimorphism.

1. Introduction

Atherosclerotic cardiovascular disease (ASCVD) is one of the leading causes of death worldwide [1]. The formation of atherosclerotic plaques depends on multiple factors, including stress, smoking, a high-fat diet, and inflammation [2]. These and other risk factors can induce endothelial dysfunction, thereby disrupting the vascular barrier [3]. As a result, circulating lipids in the form of low-density lipoproteins (LDLs) can enter and accumulate within the vessel wall, where they are oxidised by free radicals or enzymes, forming oxidised LDL (oxLDL) [4,5]. These particles further enhance endothelial cell activation, thereby stimulating the recruitment of blood leukocytes, primarily monocytes [6]. Once migrated into the vessel wall intima, monocytes differentiate into macrophages that express multiple receptors enabling oxLDL uptake and secrete pro-inflammatory cytokines, thereby further enhancing inflammation. Due to excessive lipid uptake, macrophages become foam cells, forming an atheromatous plaque [7]. During the progression of atherosclerosis, medial smooth muscle cells contribute to plaque formation through a fibroproliferative response, leading to their migration into the intimal plaque and the formation of a fibrous cap around the lipid core [6].

Elevated circulating lipid levels increase the risk of atherosclerosis, as lipid deposition within inflamed vessel walls initiates the early stages of the disease [8]. Therefore, lipid metabolism plays an essential role in the development of atherosclerosis [8]. Recent studies show that the aryl hydrocarbon receptor (AhR) plays a major role in regulating lipid metabolism [9–11]. The AhR is a cytosolic receptor best known for its role in organ detoxification. In addition to its classical ligands, exogenous compounds such as halogenated aromatic hydrocarbons or dioxins [12], endogenous metabolites, e.g., those derived from tryptophan metabolism [13], and modified LDL [14] can activate the AhR. The liver is a major metabolic organ that maintains lipid homeostasis. By regulating the uptake, storage, and conversion of lipids through exogenous and endogenous pathways, the liver's lipid metabolism also influences plasma lipid levels, which may contribute to the development of atherosclerosis [8]. It has been shown that the AhR plays a versatile role within different liver pathologies, such as metabolic dysfunction-associated steatohepatitis (MASH) or alcoholic liver disease. However, the effects range from disease-promoting to disease-attenuating, targeting distinct inflammatory, stress-related, or pro-fibrotic mechanisms in each disease [15]. Moreover, a few studies suggest that AhR activation in the liver might also play a role in lipid metabolism, for example, by interfering with the expression of fatty acid synthase (FAS) and sterol regulatory element-binding protein-1c (SREB-P1c) [16].

In addition to the liver, the small intestine is a major site of lipid metabolism [17]. Enterocytes take up predigested dietary lipids and metabolise them, secreting the resulting products into the lymphatic system, thereby making them available in the circulation [17]. Given that a few studies suggest that intestinal activation of the AhR, e.g., by bacterial metabolites, can also affect diseases related to lipid dysregulation, such as MASLD [18], we sought to investigate the precise role of the AhR in enterocytes in local lipid metabolism and its systemic effects.

In a previous study, we showed that a whole-body genetic deficiency of *Ahr* led to reduced atherosclerosis development, coinciding with lower plasma and hepatic lipid levels [9]. However, as the AhR is primarily expressed in hepatocytes but also in small intestinal epithelial cells [15,19,20], it remained unclear which role hepatic and small intestinal epithelial cell-specific AhR might play in these observations. To elucidate the regulatory effects of the AhR in hepatocytes and small intestinal epithelial cells (IECs), which are major players in lipid metabolism, we conducted mouse studies using a specific genetic aberration of *Ahr* in these cells.

2. Materials & methods

2.1. Animals

$Ahr^{fl/fl}$ mice were crossbred with $Villin^{Cre+}$ mice to generate $Ahr^{fl/fl}$ $Villin^{Cre+}$ mice (Jackson Laboratory; B6N.Cg-Tg(Vil1-cre)20Syr/J; Strain #: 033019). To generate hepatocyte-specific *Ahr*-deficient mice, $Ahr^{fl/fl}$ mice were injected with *AAV8-Albumin*^{iCre} or empty *(e)AAV8* particles for the control group (1×10^{11}). Both males and females were used for all experiments. $Ahr^{fl/fl}$ and $Ahr^{fl/fl}$ $Villin^{Cre+}$ as well as adeno-associated virus 8 *(AAV8)-Albumin*^{iCre} $Ahr^{fl/fl}$ mice were injected with proprotein convertase subtilisin/kexin type 9 (PCSK9)-D337Y overexpressing AAV8 particles. One week after the injection, at a starting age of 8 weeks, the mice were fed a high-fat diet (HFD) containing 21% fat & 0.20% cholesterol (Sniff TD88137) for 12 weeks. After euthanising by injecting ketamine (0.1 mg/g body weight) and xylazine (0.02 mg/g body weight) intraperitoneally, blood was taken via puncture of the retroorbital plexus. The vasculature was flushed with ice-cold phosphate-buffered saline (PBS), and the relevant organs were collected. All animal studies were approved by the Governmental Animal Care and

Use Committee (Landesamt für Natur, Umwelt und Verbraucherschutz Nordrhein-Westfalen, Germany, approval number 81-02.04.2019. A363). The analysis of mouse data was performed in a blinded manner.

2.2. Atherosclerotic lesions

After fixating the hearts in 4% paraformaldehyde (PFA), the tissue was embedded in Tissue-Tek O.C.T. compound (Sakura) for transverse cryo-sectioning, where 5 μm sections were cut. Aortic arches were embedded in paraffin after fixation with 4% PFA and cut into 5 μm thick sections. Hematoxylin-Eosin staining was used for overall plaque size quantification, and collagen was stained with Masson's trichrome staining, which was also used for necrotic core content analysis. An immunofluorescent staining of galectin 3 (Mac2) was used for the identification of macrophage infiltration. Antigen retrieval was performed by incubation in citrate buffer, followed by blocking with PBS containing 0.01% bovine serum albumin (BSA) and 0.0125% horse serum. The mac2 antibody (anti-mouse mac-2 antibody, Cedarlane), diluted 1:400 in PBS containing 0.015% of the blocking solution, was incubated overnight at 4°C. As a secondary antibody, DL488 goat anti-rat diluted 1:750 was incubated for 1 h at room temperature. Nuclei were stained with Hoechst 33342 solution (ThermoFisher). Mounting was performed with Thermo Scientific Fluoromount-G (ThermoFisher). Sections were imaged using Leica DMLB microscope and a charge-coupled device camera. The analysis and quantification were performed with ImageJ and QuPath [21]. For each mouse, the average of three sections was calculated per staining and tissue.

2.3. Flow cytometry

EDTA-buffered blood was pre-treated with Erythrocyte lysis buffer (150 mM NH4Cl; 10 mM KHCO3; 0,1 mM diNaEDTA) for 20 min. Hanks-buffer (HBSS, 0.06% 0.5 M EDTA, 0.6% BSA, pH 7.4) was added to stop the lysis. The blood was incubated with the following antibody mix: CD45 (APC-y7, Invitrogen), CD115 (FITC, Invitrogen), Gr1 (V500, Biolegend), B220 (eF450, Invitrogen), CD3 (PerCP, Invitrogen), all diluted 1:100. Flow cytometric analysis was performed using a FACS CantoTM II and FACS Diva software (BD Biosciences). The gating of the different populations was performed as follows: total leukocytes ($CD45^+$), classical monocytes (CD45+CD115+GR1+), B cells (CD45+CD115-GR1-B220+), $CD3^+$ T cells (CD45+CD115-GR1-$CD3^+$). Cell populations and marker expression were analysed with FlowJo 10.0 (BD Bioscience). Total cell counts were calculated using CountBright Absolute Counting Beads, according to the manufacturer's protocol.

2.4. Cholesterol & triglyceride measurement

Cholesterol and triglyceride levels in either plasma or tissue lysates were determined using enzymatic assays (Roche diagnostics) according to the manufacturer's protocol.

2.5. RNA isolation, library preparation, and sequencing

Total RNA was isolated from duodenum tissue samples (n = 4 per sex) using the miRNeasy Mini Kit (Qiagen) according to the manufacturer's protocol. Trizol was used as a lysis reagent, and an on-column DNA digestion step was performed to remove genomic DNA. Initial RNA concentration was measured using the Nanodrop One Microvolume UV-Vis Spectrophotometer (ThermoFisher Scientific). RNA integrity was assessed using the Agilent TapeStation RNA Screen Tape Assay, and concentration was precisely quantified using the Qubit RNA assay. Sequencing libraries were generated from total RNA using the QuantSeq 3′ mRNA-Seq Library Prep Kit FWD for Illumina (Lexogen), following the manufacturer's standard protocol. To enable accurate transcript quantification and remove PCR duplicates, the UMI (Unique Molecular Identifier) add-on Kit (Lexogen) was utilized. ERCC RNA Spike-in Control Mixes were added to the samples for normalization. The prepared libraries were sequenced on an Illumina NextSeq 500 system using the Mid Output v2.5 kit (150 cycles) to generate single-end reads.

2.6. Bioinformatic analysis

Sequencing reads were mapped to the Ensembl reference mouse transcriptome GRCm39 cDNA (v113) using kallisto (v0.51.1) [22] and were subsequently quantified as read counts and tpm at the gene level by the R package tximport (v1.34.0) [23] based on the Ensembl GRCm39 v113 GTF annotation file. Genes with an average expression count <5 across samples or annotated as non–protein-coding were excluded from downstream analyses. Differential gene expression analysis was performed using DESeq2 (v1.46.0) [24] with a significance threshold of $\alpha = 0.05$. Significance was defined by adjusted *P* values. Gene Ontology–based overrepresentation analysis and gene set enrichment analysis (GSEA), the latter using the Molecular Signatures Database (MSigDB) Hallmark gene sets [25] were performed using clusterProfiler (v4.14.3) [26–28]. Variance-stabilizing transformation was applied to normalize gene counts, followed by principal component analysis (PCA) to examine sample-level variation using the R package pcaMethods (v1.98.0) [29]. The RNA sequencing data have been deposited in the Gene Expression Omnibus (GEO) and are publicly available under accession number GSE314205.

2.7. Tissue lysis

Tissue lysates were produced by lysing snap-frozen tissue in M-PER™ Mammalian Protein Extraction Reagent (ThermoFisher Scientific) containing 1% Halt™ Protease Inhibitor Cocktail (ThermoFisher Scientific) and 1% Halt™ Phosphatase Inhibitor Cocktail (ThermoFisher Scientific). After a homogenization step in the TissueLyser LT (Qiagen) with a metal bead for mechanic disruption for 5 min at 50 Hz, the lysates were sonicated in a sonicator bath for 5 min. Protein concentrations were measured using the Nanodrop One Microvolume UV-Vis Spectrophotometer (ThermoFisher Scientific).

2.8. Western blotting

For Western blot analysis, 40 μg of protein lysate was separated on a 4-15% gradient gel before transfer to a nitrocellulose membrane. Antibodies were used at 1:1000 dilution: CD36 (#NB400; Novus Biologicals), SREBP-1 (sc-367; Santa Cruz Biotechnology), and GAPDH (#51332; Cell Signaling Technology). HRP-conjugated anti-rabbit IgG antibodies were used at 1:1000 dilution as secondary antibodies. Western blots were detected using an iBright 1500 (Invitrogen).

2.9. Kinase profiling

Tyrosine kinase profiles of duodenal tissue lysates (n = 4 per sex, same samples as for RNA sequencing) were determined using the PamChip® peptide tyrosine kinase microarray system on PamStation®12 (PTK; PamGene International, 's-Hertogenbosch, The Netherlands). Each PTK-PamChip® array contains 196 individual phospho-site(s) that are peptide sequences derived from substrates for tyrosine kinases. Each peptide on the chip builds a 15-amino acid sequence representing a putative endogenous phosphorylation site which functions as a tyrosine kinase substrate. The phosphorylation of the peptides is visualized by detection of the fluorescent signal which is emitted as a result of the binding of the FITC-conjugated PY20 anti-phosphotyrosine antibody. For the PTK assay, 10.0 μg of protein was applied per array and carried out using the standard protocol supplied by Pamgene. All reagents used for PTK activity profiling were supplied by Pamgene International B.V. Initially, to prepare the PTK Basic Mix, the freshly frozen lysate was added to 4 μL of 10 x protein PTK reaction buffer (PK), 0.4 μL of 100 x

bovine serum albumin (BSA), 0.4 μL of 1 M dithiothreitol (DTT) solution, 4 μL of 10 x PTK additive, 4 μL of 4 mM ATP and 0.6 μL of monoclonal anti-phosphotyrosine FITC-conjugate detection antibody (clone PY20). The total volume of the PTK Basic Mix was adjusted to 40 μL by adding distilled water (dH2O). Before loading the PTK Basic Mix onto the array, a blocking step was performed by applying 30 μL of 2% BSA to the centre of each array and then washing with PTK solution for PamChip® preprocessing. Next, 40 μL of PTK Basic Mix was applied to each array of the PamChips®. After incubation for an hour (30°C), where the sample is pumped back and forth through the porous material to maximise binding kinetics and minimise assay time, a FITC-conjugated antibody is used to detect the phosphorylation. Then, the microarray assays were run for 94 cycles. An image was recorded by a CCD camera, PamStation®12, during kinetic read cycles 32–93 at 10, 50, and 200 ms, and at the end-level read cycle at 10, 20, 50, 100, and 200 ms. The spot intensity at each time point was quantified (and corrected for local background) using the BioNavigator software version 6.3 (PamGene International, 's-Hertogenbosch, The Netherlands). Upstream Kinase Analysis (UKA) [30], a functional scoring method (PamGene) was used to rank kinases based on combined specificity scores (based on peptides linked to a kinase, derived from 6 databases) and sensitivity scores (based on treatment-control differences).

Serine-Threonine kinase profiles of duodenal tissue lysates (n = 4 per sex, same samples as for RNA sequencing) were determined using the PamChip® Ser/Thr Kinase assay (STK; PamGene International, 's-Hertogenbosch, The Netherlands). Each STK-PamChip® array contains 144 individual phospho-site(s) that are peptide sequences derived from substrates for Ser/Thr kinases. For the STK assay, each array was loaded with 2.0 μg of protein and 400 μM ATP along with an STK Basic Mix, consisting of 1 x protein PTK reaction buffer (PK), 1 x bovine serum albumin (BSA) and 1 x STK antibody mix. Prior to loading the STK Basic Mix onto the arrays, a blocking step was performed using 30 μL of 2% BSA followed by washing with PTK solution for preprocessing. Subsequently, 40 μL of STK Basic Mix was applied to each array. A FITC-conjugated antibody was applied to visualise phosphorylation after 1 h of incubation at 30°C. During this incubation, samples were pumped back and forth through the porous material to enhance binding kinetics and reduce assay duration. Imaging was performed using an LED-based imaging device, and spot intensities were measured at each time point after adjusting for local background using the BioNavigator software as described above.

Over-representation analyses (ORA) of Gene Ontology, KEGG, and WikiPathway for the kinases with significant differences from baseline were performed using the ClusterProfiler R-package [31]. The list of kinases of interest contains the kinases with higher median final scores (>1.2). For the GO enrichment analysis, we only selected the Biological Process (BP) terms and filtered out redundantly enriched GO terms by selecting only the terms with the lowest adjusted p-value from all redundant terms. The redundant terms were defined as the GO terms which have similarities higher than 0.7. The p-values were adjusted for multiple comparisons by false discovery rate (FDR).

Principal Component Analysis (PCA) was conducted to explore patterns of variation and clustering among samples based on peptide phosphorylation profiles. The analysis was performed using the stats package [32] in R, which applies singular value decomposition to the centred and scaled data matrix to examine covariances and correlations between samples. To visualise the results, ggplot2 [33] was used to generate two-dimensional PCA plots, highlighting sample distribution along the principal components. These visualisations enabled the identification of sample grouping, variability, and potential outliers.

To visualise the classification and distribution of kinases identified in the assay, a kinase coral tree was generated. This approach groups kinases based on their evolutionary and functional relationships into families and subfamilies, providing a hierarchical representation of kinase activity profiles. The kinase tree was constructed using the Coral web tool (http://phanstiel-lab.med.unc.edu/CORAL), which allows the mapping of user-defined kinase lists onto a curated phylogenetic tree based on kinase domain homology. Input data included the list of kinases detected as active in the PTK PamChip® assays. The kinases were grouped into their respective families according to the classification system provided by the Human Kinome Project. Visualization parameters were adjusted to reflect relative kinases; here, node/branch colors represent mean kinase statistics (<0.05), and node sizes represent the median final scores (>1.2). The resulting coral tree was used to assess family-wide trends, highlight condition-specific kinase activation patterns, and support the functional interpretation of the dataset.

2.10. Kinase network

A directed enzyme-to-substrate reference network was assembled by integrating multiple curated resources covering kinase–substrate and other signaling interactions: OmniPath [34], HPRD [35], PhosphoSitePlus [36], Phospho.ELM [37], Reactome [38] and DEPOP [39]. To characterise the immediate network context of kinases with significantly altered activity in the kinase profiling assay, we extracted for each such kinase its direct downstream neighbourhood. These local neighbourhoods were used to describe the direct wiring around the experimentally perturbed kinases. To account for altered kinase activity beyond direct neighbours and to quantify how strongly individual kinases may contribute to the activity pattern in the network, we applied a network propagation procedure to compute a kinase-specific contribution score. Significantly altered kinases were used as seed nodes and initialised with their measured activity change. Activity was then iteratively propagated along the directed enzyme–substrate edges, with each step transferring only a fixed fraction of the signal (geometric decay of 0.7 with path length) and propagation restricted to short paths so that only near-local signalling cascades contributed. For each seed kinase, it was calculated how much of its activity was transferred to downstream nodes, yielding a per-seed contribution score. To prioritise kinase–substrate pairs that are supported by physical proximity (direct or 1-hop), a structure-based protein–protein interaction (PPI) pipeline was implemented similar as described previously [40]. Briefly, kinase interaction candidates were first collected from the BioGRID database [41]. Direct PPI confidence for these pairs was then predicted with AlphaFold-Multimer in a high-throughput batch mode based on the ColabFold notebook v1.5.5 [42,43]. For each predicted complex the interface PAE (iPAE) metric was calculated as the mean PAE over all residues in that interface. The final PPI confidence score for each interaction was calculated as the mean of the actifpTM (actual interface pTM) score [44] and the iPAE, averaged over the five predicted interaction models. Before combination, the actifpTM score was used directly on its native 0–1 scale, whereas the iPAE was converted to a 0–1 confidence score by assigning values ≤ 5 Å to 1, values > 15 Å to 0, and linearly scaling intermediate values; the two metrics were then combined with equal weighting. These PPI confidence scores were used as an additional edge weight to preferentially amplify structurally supported kinase-substrate interactions in the kinase network propagation. All used scripts were run in Python 3.11 with pandas 2.3.3, numpy 1.24.3, networkx 3.4.2, requests 2.32.3 and scipy 1.13.1. Source code will be made available in a public GitHub repository upon publication or on reasonable request.

2.11. Small intestine organoid isolation & cell culture

Small intestine organoids were generated by isolating small intestinal crypts from the full length of the small intestine of either male or female $Ahr^{fl/fl}$ $Villin^{Cre+}$ or $Ahr^{fl/fl}$ mice and differentiating them into organoids. The isolation and cultivation were performed according to publicly available protocols from STEMCELL Technologies using the materials listed in those protocols. Passaging was performed after 7 days in culture, and experiments on the organoids were performed after at least one passage after the isolation.

For estrogen treatment, fully differentiated organoids were used and

incubated for 24h with 0.1 μM estrogen or v/v ethanol for vehicle control.

2.12. RNA isolation and PCR

RNA isolation from organoids was performed according to the STEMCELL Technologies protocol to remove the Matrigel. Lysis was performed, and further RNA isolation was performed using the Zymogen Quick RNA Micro prep Kit (Zymogen), including a step for genomic DNA digestion. Liver and intestine (Duodenum) RNA was isolated using the miRNAeasy kit (Qiagen), including a step for genomic DNA digestion, following the manufacturer's protocol. RNA concentration was measured using the Nanodrop One Microvolume UV-Vis Spectrophotometer (ThermoFisher Scientific). M-MLV reverse transcriptase (Invitrogen) was used for reverse transcription. qRT-PCR was carried out using PowerUp™ SYBR™ Green Mastermix (Thermo Fisher Scientific) in the QuantStudio 3 (QS3, Thermo Fisher Scientific) PCR system. Specificity of primer amplification was confirmed by melt curve analysis. The relative mRNA expression was calculated using the 2-ddCt method with *b-actin* used as a reference gene. The following primer sequences were used:

b-Actin-Fw (CTAAGGCCAACCGTGAAAAG), *b-Actin-Rv* (ACCAGAGGCATACAGGGACA), *Cd36-Fw* (GCCAAGCTATTGCGACATGA), *Cd36-Rv* (AAAAGAATCTCAATGTCCGAGACTTT), *Sreb-f1-Fw* (GGCACTGAAGCAAAGCTGAAT), *Sreb-f1-Rv* (CGTCTCCACCACTTCGGGTT), *Acot1-Fw* (CCCCCTTACTTCCCGCTGTG), *Acot1-Rv* (ACCTTTCCCCAACCTCCAAACC), *Plpp2-Fw* (GCAGCCCTGCTAATGTCACG), *Plpp2-Rv* (GGCCTGCACATATAGCGCC), *Hsd17b13-Fw* (AAACCCGAGTACAAGGTTATGGC), *Hsd17b13-Rv* (CGCTTTTAAGGCACGCTCAGG), *Ahr-Fw* (AAAGTCCACCCCTGCTGACA), *Ahr-Rv* (AAGCCATTCAGCGCCTGTAAC), *Cyp1a1-Fw* (TGAAGGTGGTAGTTCTTGGAGC), *Cyp1a1-Rv* (CATGATCTAGGTGGCTGCTTGG), *Tiparp-Fw* (AGAAGCCAACTCTCGGGGTC), *Tiparp-Rv* (GAACCCCACCAAGTGTCTGTAA), *Abca1-Fw* (*CCCAGAGCAAAAAGCGACTC*), *Abca1-Rv* (*GGTCATCATCACTTTGGTCCTTG*), *Acat2-Fw* (*ACCAATTCCAGCCATAAAGCA*), *Acat2-Rv* (*GGTTTAATCCAAGTTCTTTAGCTATTGC*), *Fabp1-Fw* (TGGGGAAAAAGTCAAGGCAGTCG), *Fabp1-Rv* (CAATGTCGCCCAATGTCATGGT), *Fabp2-Fw* (TCTAGCAGACGGAACGGAGC), *Fabp2-Rv* (ACTCCTTCATATGTGTAGGTCTGG), *Srb1-Fw* (AAGGGCATCGGGCAAACAG), *Srb1-Rv* (AGCCCTTTTTACTACCACTCCA), *Ppard-Fw* (CGGACCTGGGGATTAATGGGA), *Ppard-Rv* (CGCAGATGGACTGCCTTTACCG), *Pparg-Fw* (CCACCAACTTCGGAATCAGCT), *Pparg-Rv* (TTTGTGGATCCGGCAGTTAAGA), *Fatp4-Fw* (GAGGCTGAGTCTCGGCACAA), *Fatp4-Rv* (ACCTGGGGGATGTGGAAACG), *Dgat1-Fw* (GTAGAAGAGGACGAGGTGCGAG), *Dgat1-Rv* (CCTTGCATTACTCAGGATCAGCA), *Dgat2-Fw* (AGCATCCTCTCAGCCCTCCAA), *Dgat2-Rv* (ACTGCGATCTCCTGCCACCTTTC), *Npc1-Fw* (CATGTAGCTGCCAGGACTGC), *Npc1-Rv* (ACAAAGTACCGCCTTCTGTGGC), *Npc1l1-Fw* (CCTGGTGGACTGGAAGGACC), *Npc1l1-Rv* (CGAGTAGTCCGTCCCTTGGT), *Pla2g12b-Fw* (GAGCCCAATGGTTGCAGTTC), *Pla2g12b-Rv* (AATCACAGGCTGCTTCCACG).

2.13. Multiplex-bead-array

Mouse plasma was analysed for various cytokines using the “Mouse ProcartePlex Mix&Match” (Thermo Fisher Scientific (eBioscience)). Sample preparation and analysis were performed according to the manufacturer's protocol. The kit allows the simultaneous detection and quantification of soluble murine IL-6, TNF, RANTES (CCL5), GRO-α (CXCL1), ENA-78 (CXCL5), and IP-10 (CXCL10). The bead-based assay follows the principles of a sandwich immunoassay. Fluorescent magnetic beads are coupled with antibodies specific to the analytes to be detected. Beads are differentiated by their sizes and distinct spectral signature (colour-coded) by flow cytometry using the Luminex™ xMAP, data were collected with the xPONENT software (Thermo Fisher Scientific, v.4.2) and analysed with the ProcartaPlex Analyst software (Thermo Fisher Scientific, v.1.0).

2.14. Statistics

Statistical analyses were conducted using GraphPad Prism 10 (GraphPad Software Inc.). Gaussian normality of data distribution was assessed using the Shapiro-Wilk test, and outliers were identified with the ROUT test. In accordance with the ARRIVE guidelines, all animals were included in the analysis, except for those identified as statistically defined outliers. Depending on data distribution, comparisons between two groups were made using either the unpaired two-tailed Student's t-test with Welch's correction or the Mann-Whitney *U* test, as appropriate. Comparisons among three groups were made using an ordinary two-way ANOVA with Tukey's multiple comparison test. A two-tailed P value < 0.05 was considered statistically significant. Genotype-by-sex interaction was assessed by ordinary two-way ANOVA. Data are represented as mean ± standard error of mean (SEM). $^{*}P < 0.05$, $^{**}P < 0.01$, $^{***}P < 0.001$.

3. Results

3.1. Hepatocyte-specific deficiency of the Ahr does not influence lipid metabolism and atherosclerosis development

In a previous study in mice with whole-body *Ahr* deficiency in an atherosclerotic setting, we observed that *Ahr* deficiency led to a significant reduction in plasma and liver lipid levels, resulting in reduced plaque development [9]. To investigate whether this process is hepatocyte-driven, we injected $Ahr^{fl/fl}$ mice with an Albumin Cre-containing adeno-associated virus 8 (AAV8) and an AAV8 encoding PCSK9 overexpression and fed them an HFD for 12 weeks (Fig. 1A). After validating knockdown of *Ahr* and AhR-mediated signalling (Supplementary Fig. 1), we unexpectedly observed no changes in plasma or hepatic cholesterol or triglyceride levels (Fig. 1B–E). Additionally, we measured plaque size in the aortic roots and arches but did not observe any effect of hepatic *Ahr* deficiency (Fig. 1F–I). Characterisation of the plaques also revealed no significant changes in collagen or necrosis content within the plaques; the percentage of Mac2-positive macrophages did not change (Supplementary Fig. 2A–B). To investigate potential inflammatory effects of hepatic *Ahr* deficiency, we measured circulating leukocyte levels and hepatic cytokine levels, which remained unaffected (Supplementary Fig. 2C–D). Based on these findings, we suggest that in our specific experimental model, the hepatocyte-specific *Ahr* is not primarily involved in lipid metabolism or in the development of atherosclerosis.

3.2. Lack of Ahr in intestinal epithelial cells leads to downregulated intestinal lipid metabolism, specifically in male mice

Since it has already been reported that intestinal AhR may contribute to dyslipidemia-driven diseases such as MASLD [45], we investigated whether the AhR in IECs regulates lipid metabolism and thereby contributes to the observations in the whole-body *Ahr*-deficient model [18]. We therefore created an IEC-specific *Ahr*-deficient mouse model by crossing $Ahr^{fl/fl}$ with $Villin^{Cre+}$ mice. To induce dyslipidemia, mice were injected with AAV8 encoding PCSK9 and fed an HFD for 12 weeks (Fig. 2A). After validating knockdown of *Ahr* and AhR-mediated signalling (Supplementary Fig. 3), we interestingly found that only male mice lacking *Ahr* in IECs exhibited significantly reduced plasma cholesterol and triglyceride levels, whereas female mice showed no changes in plasma lipid levels (Fig. 2B–C; Genotype-by-sex interaction: $P = 0.0009$ (2B) and $P = 0.036$ (2C)). Similarly, in the livers of these mice, we observed significantly lower cholesterol levels in male IEC-specific *Ahr*-deficient mice compared with male controls, while triglyceride levels remained relatively unaffected (Supplementary Fig. 4A–B). To determine whether lipid levels were also altered in the intestines, we measured cholesterol and triglyceride levels in the mice's duodenal tissue lysates. Consistent with plasma lipid levels, we observed

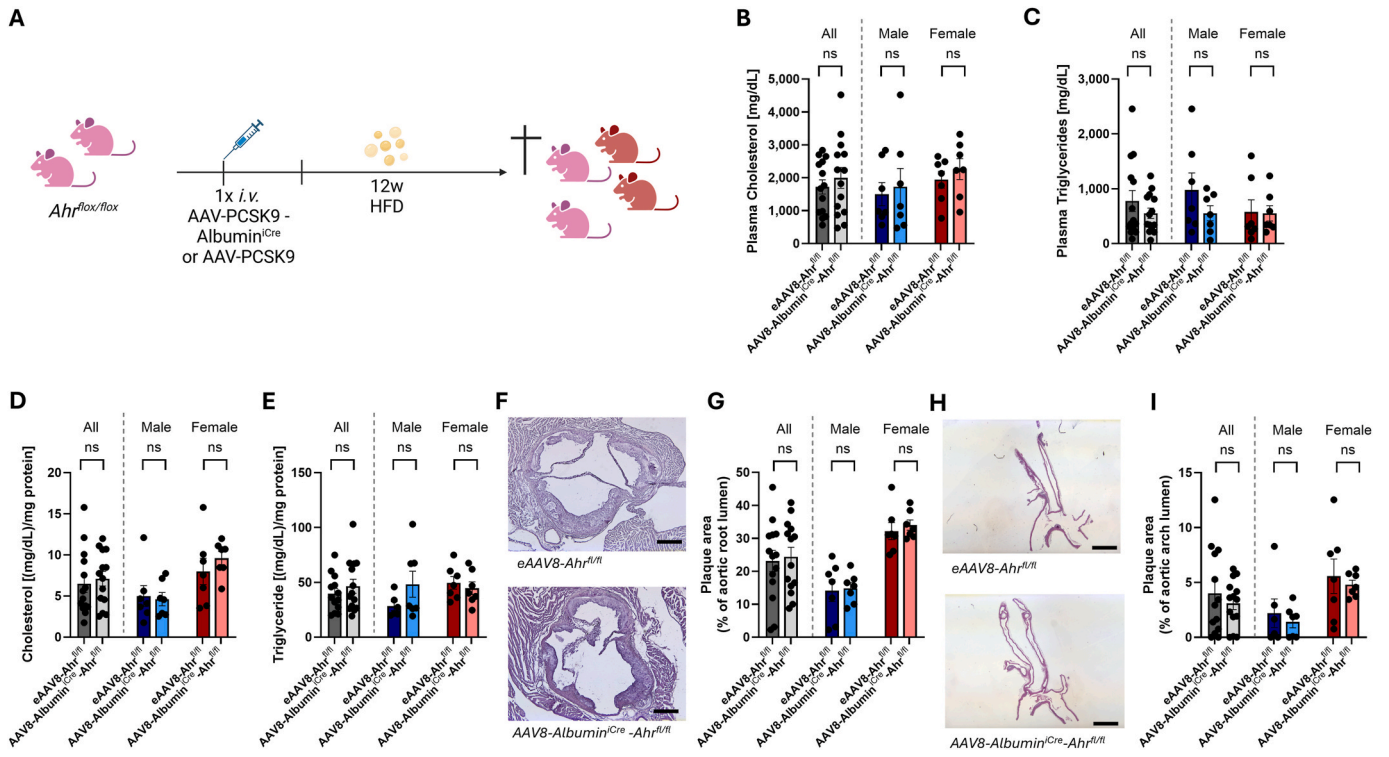

Fig. 1. Hepatocyte-specific *Ahr* deficiency does not affect lipid levels and atherosclerosis. **(A)** Schematic overview of experimental mouse breeding and experiment of *AAV8-Albumin*^{iCre}*-Ahr*$^{fl/fl}$ and *eAAV8-Ahr*$^{fl/fl}$ mice with a 12-week HFD. **(B–C)** Plasma cholesterol (B; Combined n = 14, male n = 7, female n = 7) and plasma triglyceride (C; Combined n = 14, male n = 7, female n = 7) levels. **(D–E)** Liver cholesterol (D; Combined n = 14, male n = 7, female n = 7), and triglyceride (E; Combined n = 13 (*eAAV8-Ahr*$^{fl/fl}$) or n = 14 (*AAV8-Albumin*^{iCre}*-Ahr*$^{fl/fl}$), male n = 6 (*eAAV8-Ahr*$^{fl/fl}$) or n = 7 (*AAV8-Albumin*^{iCre}*-Ahr*$^{fl/fl}$), female n = 7) levels. **(F–G)** Representative pictures of HE-stained aortic roots (F; scale = 200 μm) and quantification of plaque content (G; Combined n = 14, male n = 7, female n = 7). **(H–I)** Representative pictures of HE stained aortic arches (H; scale = 2 mm) and quantification of plaque content (I; Combined n = 13 (*eAAV8-Ahr*$^{fl/fl}$) or n = 14 (*AAV8-Albumin*^{iCre}*-Ahr*$^{fl/fl}$), male n = 6 (*eAAV8-Ahr*$^{fl/fl}$) or n = 7 (*AAV8-Albumin*^{iCre}*-Ahr*$^{fl/fl}$), female n = 7). Graphs represent mean ± SEM.

markedly reduced duodenal triglyceride levels in IEC-specific *Ahr*-deficient mice, although there is no definitive evidence for a different genotype effect between sexes. The intestinal cholesterol level, however, was not affected (Fig. 2D–E; Genotype-by-sex interaction: $P = 0.87$ (2D) and $P = 0.51$ (2E)). Next, we performed RNA sequencing of the intestinal tissue to identify potential mechanisms driving alterations in lipid levels. We discovered that male *Ahr*$^{fl/fl}$ *Villin*$^{Cre+}$ mice exhibited lower expression of genes involved in lipid metabolism, such as *Cd36* and sterol regulatory element-binding transcription factor 1 (*Srebf1*), among a wide range of other differentially regulated genes (Fig. 2F). In line with our previous findings, in female mice, RNA sequencing revealed that the genetic aberration of the *Ahr* in intestinal epithelial cells did not lead to any major transcriptional changes (Fig. 2G), underscoring unaffected lipid levels in the intestine and plasma. This sex-effect on the transcriptome level is *Ahr*-dependent as no major changes were observed between wildtype (*Ahr*$^{fl/fl}$) male and female mice, but only between *Ahr*$^{fl/fl}$ *Villin*$^{Cre+}$ mice (Supplementary Fig. 5A). In a Principal Component Analysis, it became further evident that the impact of the genetic aberration in male mice is substantially greater than in female mice, resulting in markedly different male phenotypes in the absence of *Ahr* (Fig. 2H).

To further unravel the targeted genes, we identified the top 20 up- & down-regulated genes in male mice lacking *Ahr* compared with their controls. In the top-downregulated genes, we found five genes that are involved in lipid metabolism: phospholipid phosphatase (*Plpp2*), *Hsd17b13*, acyl-CoA thioesterase (*Acot1*), sterol regulatory element-binding protein 1 (*Srebf1*), and *Cd36*, suggesting that the *Ahr*-deficiency in IECs affects lipid metabolism by impacting the transcription of these lipid-related genes (Fig. 2I and Supplementary Fig. 5B). Additionally, we could demonstrate that CD36 and SREBP1 (encoded by *Srebf1*) protein levels seemed to be reduced in the duodenum of male mice lacking *Ahr* in IECs (Supplementary Fig. 5C and Supplementary Fig. 6). To obtain more detailed information on which lipid-metabolic processes are altered, we selected genes associated with diverse intestinal lipid characteristics and performed RT-qPCR on duodenal tissue from male mice. Here, we found that, in particular, genes assigned to intracellular lipid transport (i.e. *Fabp2*, *Abca1*), fatty acid metabolism (i.e. *Fatp4*), and chylomicron formation (i.e. *Pla2g12b*) were downregulated (Supplementary Fig. 5D).

To identify if the transcriptional effects are mediated by the *Ahr* in IECs on a baseline level, we cultured small intestinal organoids, composed of epithelial cells and their respective stem cells [46], which originated from male *Ahr*$^{fl/fl}$ *Villin*$^{Cre+}$ or *Ahr*$^{fl/fl}$ mice on a standard laboratory diet. The relative mRNA expression of the genes *Srebf1*, *Hsd17b13*, and *Acot1* was significantly downregulated in organoids deriving from *Ahr*$^{fl/fl}$ *Villin*$^{Cre+}$ mice in comparison to *Ahr*$^{fl/fl}$ mice (Fig. 2J). For the genes *Plpp2* and *Cd36*, the lack of the *Ahr* did not lead to a significant change in mRNA expression at baseline. These results further strengthen our suggestion that IECs lacking *Ahr* already show signs of altered lipid gene expression, which, during atherosclerosis development, is further enhanced, leading to additional transcriptional changes.

As we identified a major sex difference in the intestines, we next sought to determine whether sex hormones, such as estrogen, would affect the downstream effects of AhR. We incubated small intestinal organoids derived from male *Ahr*$^{fl/fl}$ *Villin*$^{Cre+}$ or *Ahr*$^{fl/fl}$ mice on a standard laboratory diet with estrogen or vehicle control. While in vehicle-treated cells, largely similar effects could be observed in small intestinal organoids derived from male *Ahr*$^{fl/fl}$ *Villin*$^{Cre+}$ compared to *Ahr*$^{fl/fl}$ mice as observed in Fig. 2J (untreated cells), estrogen treatment

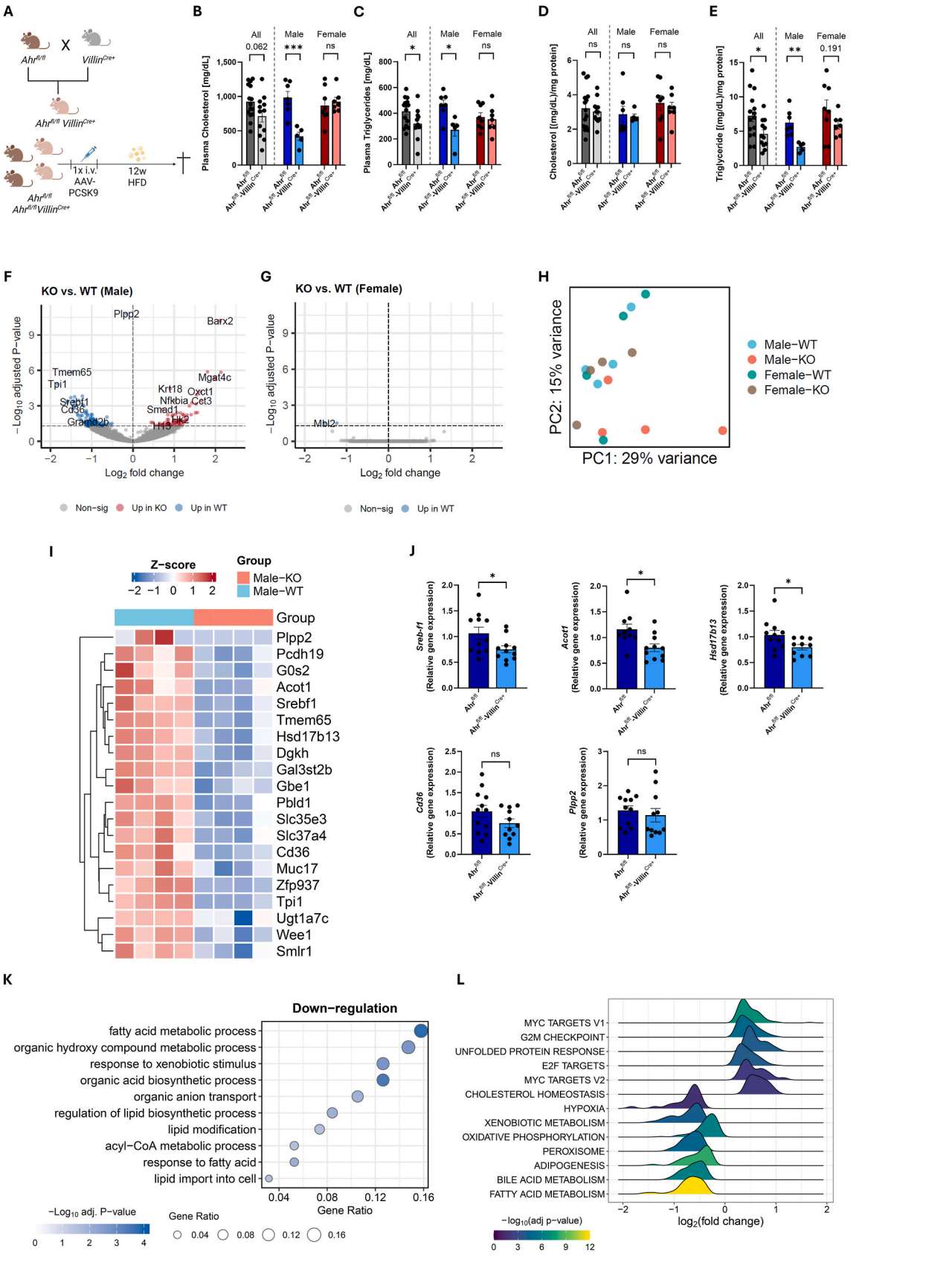

(caption on next page)

Fig. 2. Intestinal epithelial cell *Ahr*-deficient mice demonstrate an altered lipid metabolism. **(A)** Schematic overview of experimental mice breeding and experiment of $Ahr^{fl/fl}Villin^{Cre+}$ and $Ahr^{fl/fl}$ mice with a 12-week HFD. **(B–C)** Plasma cholesterol (B; Combined n = 15 ($Ahr^{fl/fl}$) or n = 12 ($Ahr^{fl/fl}Villin^{Cre+}$), male n = 7 ($Ahr^{fl/fl}$) or n = 5 ($Ahr^{fl/fl}Villin^{Cre+}$), female n = 8 ($Ahr^{fl/fl}$) or n = 7 ($Ahr^{fl/fl}Villin^{Cre+}$)) and plasma triglyceride levels (C; Combined n = 15 ($Ahr^{fl/fl}$) or n = 12 ($Ahr^{fl/fl}Villin^{Cre+}$), male n = 7 ($Ahr^{fl/fl}$) or n = 5 ($Ahr^{fl/fl}Villin^{Cre+}$), female n = 8 ($Ahr^{fl/fl}$) or n = 7 ($Ahr^{fl/fl}Villin^{Cre+}$)). **(D–E)** Duodenal cholesterol levels (D; Combined n = 15 ($Ahr^{fl/fl}$) or n = 12 ($Ahr^{fl/fl}Villin^{Cre+}$), male n = 7 ($Ahr^{fl/fl}$) or n = 5 ($Ahr^{fl/fl}Villin^{Cre+}$), female n = 8 ($Ahr^{fl/fl}$) or n = 7 ($Ahr^{fl/fl}Villin^{Cre+}$)) and duodenal triglyceride levels (E; Combined n = 15 ($Ahr^{fl/fl}$) or n = 12 ($Ahr^{fl/fl}Villin^{Cre+}$), male n = 7 ($Ahr^{fl/fl}$) or n = 5 ($Ahr^{fl/fl}Villin^{Cre+}$), female n = 8 ($Ahr^{fl/fl}$) or n = 7 ($Ahr^{fl/fl}Villin^{Cre+}$)). **(F–G)** Volcano plots of differentially regulated genes determined with RNA sequencing in the duodenum of male (F) and female (G) $Ahr^{fl/fl}$ $Villin^{Cre+}$ (KO; n = 4 per sex) vs $Ahr^{fl/fl}$ (WT n = 4 per sex) mice after a 12-week HFD. **(H)** Principal component analysis (PCA) plot of differentially regulated genes in male and female $Ahr^{fl/fl}$ $Villin^{Cre+}$ (KO; n = 4 per sex) vs $Ahr^{fl/fl}$ (WT; n = 4 per sex) mice after a 12-week HFD. **(I)** Top 20 downregulated genes in the duodenum of male mice (n = 4). **(J)** Relative mRNA expression of selected genes in small intestinal organoids isolated from male $Ahr^{fl/fl}$ (n = 10 technical replicates from n = 5 biological replicates) and $Ahr^{fl/fl}$ $Villin^{Cre+}$ (n = 10 technical replicates from n = 5 biological replicates) mice. The relative mRNA expression was calculated using the 2-ddCt method with *b-actin* used as a reference gene. **(K)** Top 10 GO pathways enriched for pathways that at least contain one of the selected genes *Plpp2, Hsd17b13, Acot1, Srebf1,* and *CD36* involved in lipid metabolism from the top differentially regulated genes in the duodenal tissue of male $Ahr^{fl/fl}$ (n = 4) vs. $Ahr^{fl/fl}$ $Villin^{Cre+}$ (n = 4) mice after a 12w HFD. **(L)** GSEA hallmark analysis of duodenal tissue of male $Ahr^{fl/fl}$ (n = 4) vs. $Ahr^{fl/fl}$ $Villin^{Cre+}$ (n = 4) mice after a 12-week HFD. Graphs represent mean ± SEM. $^{*}P < 0.05$, $^{**}P < 0.01$, $^{***}P < 0.001$.

of $Ahr^{fl/fl}$ $Villin^{Cre+}$ organoids either diminished or even over-compensated for the effects of *Ahr* deficiency on lipid-related genes. These results suggest that estrogen may interfere with the AhR and its downstream signalling (Supplementary Fig. 5E).

To investigate the metabolic impact of the differential expression of these genes, we performed a gene set over-representation analysis (GSOA) based on RNA sequencing of intestinal tissue from HFD-fed male mice. We identified pathways that at least contain one of the previously identified genes: *Plpp2*, *Hsd17b13*, *Acot1*, *Srebf1,* or *Cd36* (Fig. 2K). We found that the top three downregulated pathways of the GO analysis were fatty acid metabolic process, organic hydroxy compound-related metabolic pathways, and response to xenobiotic stimulus. Moreover, among the top ten down-regulated pathways, we found other lipid-related pathways, namely regulation of lipid biosynthetic processes, lipid modification, and lipid import into the cell, suggesting that the effects of IEC-specific *Ahr* deficiency comprise specific aspects of lipid metabolism. Furthermore, in a gene set enrichment analysis (GSEA), the top downregulated pathway was fatty acid metabolism. Additionally, xenobiotic metabolism was downregulated in $Ahr^{fl/fl}$ $Villin^{Cre+}$ mice (Fig. 2L). Interestingly, cholesterol homeostasis was significantly upregulated, indicating a separate regulation of cholesterol. Even though local effects of altered cholesterol content in the small intestine were not visible (Fig. 2D), systemic effects of altered cholesterol content appeared, which could potentially be driven by the alteration of cholesterol processing in the small intestine.

Altogether, these results suggest that the AhR in IECs of male mice plays a major role in fatty acid metabolism and cholesterol homeostasis, at least at the transcriptional level, with local and systemic effects on triglyceride levels and a proven impact on systemic cholesterol levels.

3.3. Male intestinal epithelial cell-Ahr-deficient mice exhibit an altered intestinal kinomic profile

To further elucidate the mechanisms underlying the observed changes, we performed kinase activity profiling of duodenal tissue. By quantifying the phosphorylation of known peptides, we evaluated the activity of intestinal kinases. Herein, we identified that male *Ahr*-deficient mice exhibited a significantly distinct protein tyrosine kinase (PTK) profile compared to the male control mice, with kinase activities being both up- and downregulated (Fig. 3A–D). The serine/threonine kinase (STK) profile also showed significantly altered kinomics, however, less strongly than the PTK profile (Supplementary Fig. 7A–D).

To interpret the effects of PTK regulation, we performed various pathway analyses using the kinomics data. In line with previous findings of an altered lipid metabolism in the small intestine, we also confirmed alterations of lipid-related kinase pathways in the small intestine of male IEC-specific *Ahr*-deficient mice, when compared to mice with a functional AhR in IECs. Targeted pathways included long-chain fatty acid import across the plasma membrane, regulation of fatty acid beta-oxidation, lipid metabolism pathway, negative regulation of lipid transport, regulation of lipolysis in adipocytes, and lipid and atherosclerosis (Fig. 3E). Additionally, we identified that inflammation-related pathways were significantly affected by the IEC-specific *Ahr*-deficiency, among others, leukocyte migration, leukocyte degranulation, negative regulation of leukocyte activation, regulation of leukocyte proliferation, leukocyte cell-cell adhesion, regulation of phagocytosis, and leukocyte trans-endothelial migration, confirming a major role of IEC-derived AhR activity in gut immune homeostasis (Fig. 3F). We furthermore found that many of the cytokine signalling pathways, such as interleukin 3 (IL-3), interleukin 6 (IL-6), granulocyte-macrophage colony-stimulating factor (GM-CSF) signaling, interleukin 2 (IL-2) signaling, interferon signaling, response to tumor necrosis factor, interleukin 11 (IL-11), interleukin 5 (IL-5), interleukin 7 (IL-7), and interleukin 4 (IL-4) signaling were altered on a kinase activity level, confirming an altered AhR-mediated inflammatory status in the gut (Fig. 3G).

Next, we analysed kinase activity across the selected categories (Fig. 3H). Kinases involved in lipids, inflammation, as well as cytokines, showed a negative kinase activity in $Ahr^{fl/fl}Villin^{Cre+}$ compared to $Ahr^{fl/fl}$ mice, aligning with the downregulation of lipid gene transcription as seen in Fig. 2. Interestingly, STK family kinases exhibited mixed kinase activity profiles, with those in lipid and cytokine pathways showing positive activity (Supplementary Fig. 7E). The kinases JAK2, LYN, and FYN from the PTK family, and AKT1, AKT2, and PRKACA from the STK family, were most frequently identified among the top altered pathways (Fig. 3I).

To assess the impact of the kinases involved in the previously identified lipid pathways, we subsequently performed a network analysis of the kinases that contribute to these pathways. Using the assembled kinase network, we calculated, for each lipid-pathway kinase, a contribution score that integrates its activity with the size of its reachable downstream target set across network depth (up to ten steps from the kinase). Thereby, we found that the kinases JAK2, FLT1, and FLT3 showed the highest contribution in the differentially regulated lipid pathways (Fig. 3J). Furthermore, we observed that PTKs overall show higher contribution scores than STKs. In a follow-up analysis, we additionally identified the number of direct positive or negative downstream targets of the kinases. The kinases AKT1, AKT2, and PRKACA from the STK family, which have previously been identified as the most regulated STKs, are also the top three kinases having negative downstream effects (Fig. 3K). The kinase SRC had the highest number of positive downstream targets; additionally, kinases from the STK family had fewer positive downstream targets than PTKs (Supplementary Fig. 7F). These findings suggest that the absence of *Ahr* in the IECs of male mice impacts the kinomic profile in duodenal tissue, in which PTK members with positive downstream targets are downregulated, thereby contributing to alterations in lipid pathways. Kinases of the STK family contribute less, with both up- and down-regulated activity, but regulate more positive downstream targets.

In contrast to these findings in male specimens, kinomics in female mice showed no major changes in kinase activity, underlining the previously reported findings (Supplementary Fig. 8A–F).

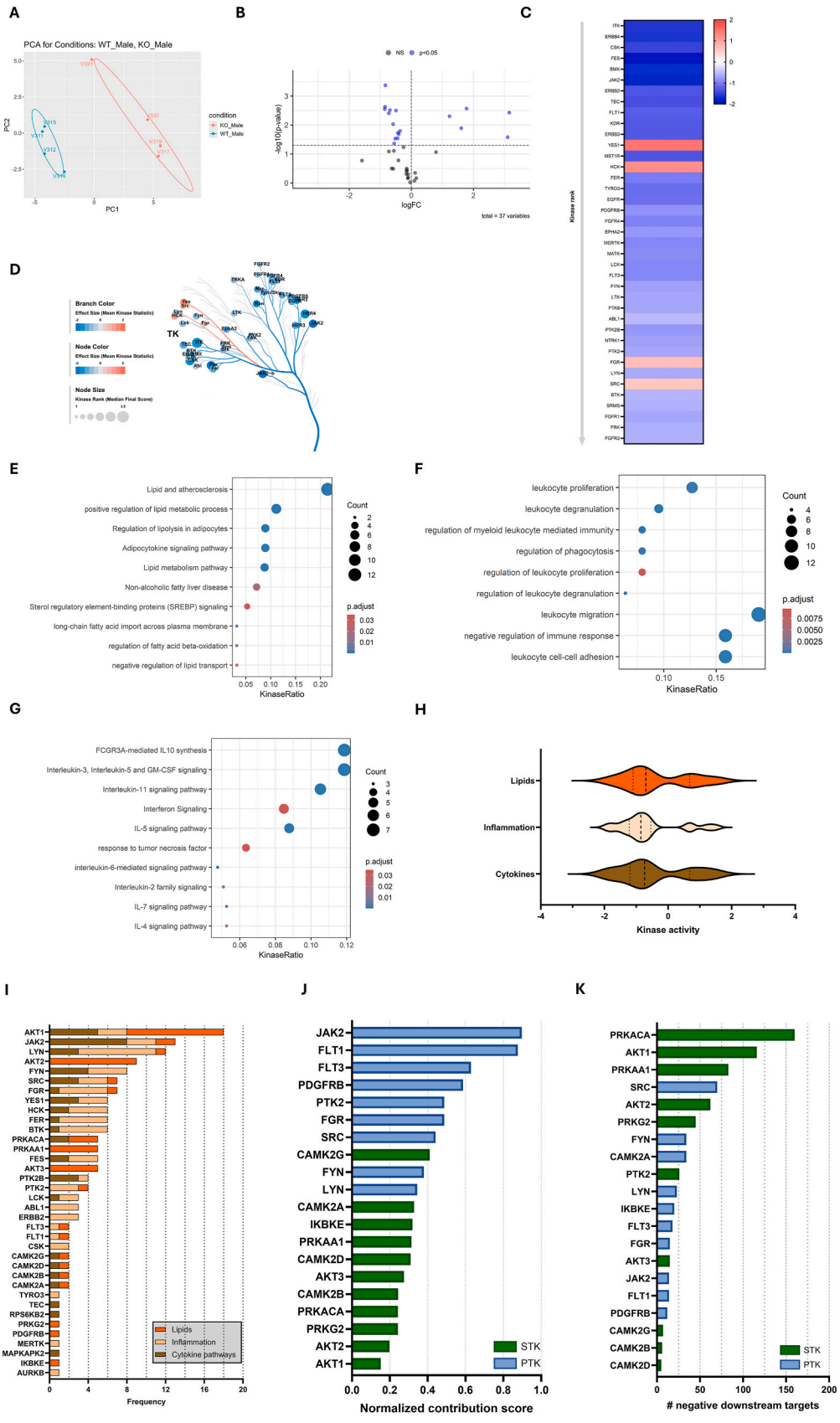

(caption on next page)

Fig. 3. Lipid and inflammation-related kinases are less active in the intestines of *Ahr*-deficient male mice. **(A–K)** Kinase profiling on intestinal lysates from male $Ahr^{fl/fl}$ $Villin^{Cre+}$ (n = 4) compared to $Ahr^{fl/fl}$ (n = 4) mice after a 12-week HFD. **(A)** Principal component analysis (PCA) depicting the variance in PTK-related peptide phosphorylation profiles. **(B)** Volcano plot displaying differentially phosphorylated PTK-related peptides. Blue dots represent significant differential phosphorylation of peptides between the two groups ($P < 0.05$). Total variables denote the number of peptides with measurable phosphorylation levels. **(C)** Heatmap showing effect size (mean kinase statistic) for PTKs, sorted based on kinase rank (mean kinase score). Blue reflects downregulated activity, while red reflects upregulated activity in intestines from $Ahr^{fl/fl}$ $Villin^{Cre+}$ compared to $Ahr^{fl/fl}$ mice, respectively. **(D)** Kinome coral tree depicting kinase rank (node size) and the effect size (node and branch color) of significantly differentially regulated kinases. **(E)** Top regulated lipid pathways. **(F)** Top regulated immunoregulatory pathways. **(G)** Top regulated cytokine pathways. **(H)** Kinase activity of PTKs involved in the selected pathway clusters, based on mean kinase statistic. Negative value reflects reduced activity in intestines from $Ahr^{fl/fl}$ $Villin^{Cre+}$ compared to $Ahr^{fl/fl}$ mice. **(I)** Bar graph of the kinase frequency among the selected pathways (e.g., a frequency of 1 denotes that the kinase is involved in one pathway, while a frequency of 5 denotes that the kinase is involved in five distinctive pathways). **(J)** Normalized contribution scores of PTKs and STKs involved in regulated lipid pathways. The contribution score is derived from network propagation on an assembled kinase–substrate network and reflects, for each kinase, how strongly its activity change may contribute to the activity of reachable downstream targets across multiple network steps (up to ten steps). **(K)** Number of negatively regulated direct downstream substrates/targets for each kinase involved in regulated lipid pathways. (For interpretation of the references to color in this figure legend, the reader is referred to the Web version of this article.)

3.4. Lack of intestinal epithelial cell-specific Ahr leads to amelioration of plaque formation

Having identified the small intestine as a site of action for lipid metabolic alterations upon *Ahr*-deficiency, we next aimed to characterise the systemic impact on the development of atherosclerosis. Therefore, we analysed lesion sizes in male mice after 12 weeks on an HFD. Consistent with the observed lipid alterations, male mice lacking *Ahr* in IECs exhibited reduced plaque size in the aortic roots and arches, with a greater reduction in the arches (Fig. 4A–D). The collagen content of plaques in the aortic roots did not change significantly in male mice, nor did the lesional necrosis (Fig. 4E–G). However, the aortic root plaques of male mice lacking *Ahr* in IECs tended to contain more macrophages than those of control mice (Fig. 4H–I).

Interestingly, when analysing atherosclerotic lesions in female mice, we observed that, despite the lack of alterations in intestinal or systemic lipid metabolism, lesion sizes in female mice lacking *Ahr* in IECs were also significantly smaller than those in controls in both aortic roots and arches, demonstrating that there is no sex-specific genotype effect (Fig. 4A–D; Genotype-by-sex interaction: $P = 0.82$ (4B) and $P = 0.87$ (4D)). Moreover, the plaques in aortic roots showed significantly less collagen and tended to contain more macrophages, while the necrosis remained unaffected (Fig. 4E–I). Given that these results were somewhat unexpected in the absence of changes in lipid levels, we measured plasma leukocyte levels as a potential driver of atherosclerosis in females. Here, we found that, specifically in female IEC-specific *Ahr*-deficient mice, circulating leukocyte levels were significantly lower than in the control group, potentially affecting lesion development. Interestingly, in the male group, there were no significant differences in any leukocyte subset, suggesting potential sex-dimorphic actions of intestinal AhR. (Fig. 4J; Genotype-by-sex interaction: $P = 0.041$ (4J; Leukocytes)). To gain further insight into the inflammatory profile of the mice and explore whether altered inflammatory signalling could contribute to the observed changes in circulating leukocytes, we measured cytokine levels in plasma. However, no changes in circulating cytokines were identified, neither in males nor in females (Supplementary Fig. 9). These results indicate that the AhR influences leukocyte homeostasis while circulating cytokine levels remain largely unaffected.

4. Discussion

The AhR is a versatile transcription factor with functions in detoxification, immunomodulation, and, more recently, lipid metabolism. In a previous study, we showed that a whole-body genetic deficiency of *Ahr* led to changes in lipid metabolism that appeared to be driven by the liver. In the present study, however, we demonstrated that these effects are unlikely to be hepatocyte-driven, as we found that the small intestinal epithelial cell AhR significantly impacts lipid metabolism in male mice, with downstream consequences for atherosclerotic plaque development.

Intestinal lipid metabolism is a complex process that involves lipid uptake, intracellular metabolism of absorbed lipids, packaging into chylomicrons and other lipoproteins, and fatty acid oxidation [17]. In our study, we identified *Ahr* in IECs as a novel mediator of intestinal lipid metabolism (at least triglycerides) in male mice. Several recent studies have focused on the role of the AhR in lipid metabolism [47–50]. For instance, it has been suggested that intestinal microbial metabolites such as lipopolysaccharide (LPS), short-chain fatty acids, and bile acids influence AhR activity and thereby alter gene transcription, with effects on, e.g., lipid peroxidation via *Cyp1a1* expression [48]. Moreover, several studies in mice with a lipid disorder that used AhR inhibition with chemical agents show improvements in the lipid phenotype, whereas chemical AhR activation has adverse effects on the disease [11], consistent with our observations. In an obesity model, disease outcome was improved by treating HFD-fed mice with α-naphthoflavone, an AhR inhibitor, which regulated the transcription of liver metabolic genes, including peroxisome proliferator-activated receptor y (*Ppary),* forkhead box protein O1 *(Foxo1),* and stearoyl-coA 9-desaturase *(Scd1)* [50]. Although this study uses an inhibitor and our model uses a genetic deficiency, both studies show a protective effect against lipid accumulation upon AhR inactivation or *Ahr* deficiency. Notably, their study also observed sex differences, with female mice showing milder effects of inhibitor treatment than male mice, findings that partly align with our observations, in which female mice did not exhibit any alterations in lipid metabolism upon *Ahr* deficiency. Vice versa, in another mouse study focusing on the effects of kynurenine, a potent AhR activator, it was shown that metabolic disorder and obesity are mediated via the AhR-signal transducer and activator of transcription 3 (STAT3)-IL-6 axis, which is highly regulated by JAK2 [51], the kinase that also has the highest contribution to the kinomic effects in our study. More precisely, in this study, genetic knockdown of *Ahr* in adipocytes led to improved lipolysis and reduced lipogenesis [49]. In line with these studies, several other studies showed similar effects: *Ahr* null ($Ahr^{-/-}$) and *Ahr* heterozygous ($Ahr^{+/-}$) mice were protected against HFD-induced obesity, with ameliorated hepatic steatosis and dyslipidaemia [52]. Another study showed that the chemical activation of the AhR by 2,3,7,8-tetrachlorodibenzodioxin (TCDD) and benzo(a)pyrene (B[a]P) could promote liver lipid deposition by inhibiting expression of Niemann-Pick disease type C1 (NPC1) intracellular cholesterol transporter 1, which seemed to be AhR-dependent [53]. Taken together, these studies align with our findings that the AhR is an essential regulator of lipid metabolism, as it aggravates lipid accumulation and thereby contributes to lipid-related disorders.

While these studies focus on different organs (e.g., the liver) and mechanisms of AhR activation, the disease outcomes are similar to those observed in our IEC deficiency model, highlighting a major impact of the AhR on lipid metabolism, which may be differentially regulated across cell types. Moreover, our study highlights the role of AhR in regulating intestinal lipid metabolism (at least triglycerides), which is most affected in male mice, and unravels new potential AhR-related intestinal target genes and kinases. Interestingly, although numerous studies have shown effects of hepatocyte-specific AhR on lipid metabolism, we did

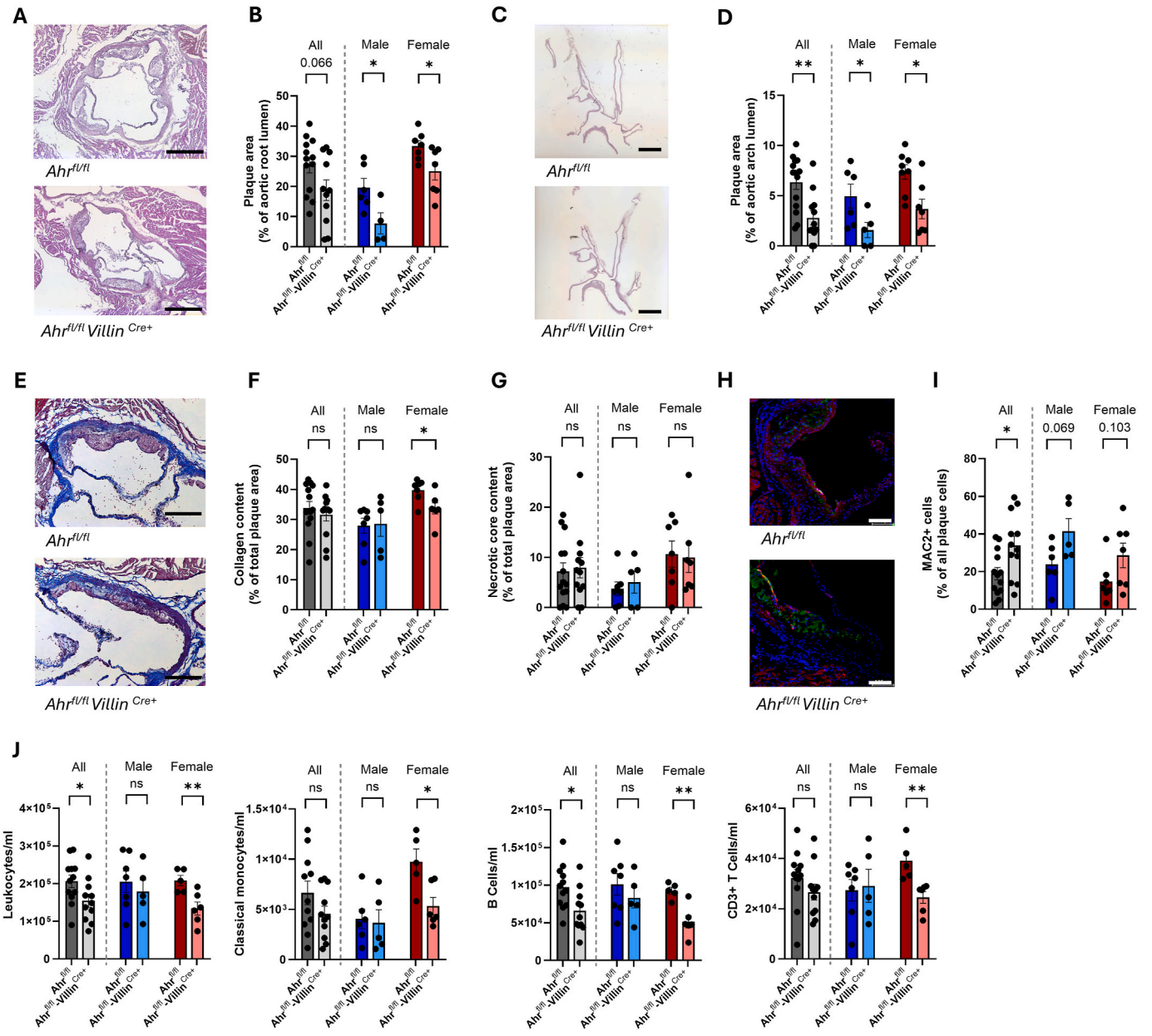

Fig. 4. Lack of intestinal epithelial cell *Ahr* results in reduced atherosclerosis development.
Ahr$^{fl/fl}$ *Villin*$^{Cre+}$ and *Ahr*$^{fl/fl}$ mice were fed a HFD for 12 weeks. **(A–B)** Representative pictures of HE stained aortic roots (A; scale = 200 μm) and quantification of plaque content (B; Combined n = 13 (*Ahr*$^{fl/fl}$) or n = 11 (*Ahr*$^{fl/fl}$*Villin*$^{Cre+}$), male n = 6 (*Ahr*$^{fl/fl}$) or n = 4 (*Ahr*$^{fl/fl}$*Villin*$^{Cre+}$), female n = 7). **(C–D)** Representative pictures of HE stained aortic arches (C; scale = 2 mm) and quantification of plaque content (D; Combined n = 14 (*Ahr*$^{fl/fl}$) or n = 12 (*Ahr*$^{fl/fl}$*Villin*$^{Cre+}$), male n = 6 (*Ahr*$^{fl/fl}$) or n = 5 (*Ahr*$^{fl/fl}$*Villin*$^{Cre+}$), female n = 8 (*Ahr*$^{fl/fl}$) or n = 7 (*Ahr*$^{fl/fl}$*Villin*$^{Cre+}$)). **(E–G)** Representative pictures of Masson trichrome-stained aortic roots (E; scale = 100 μm) and quantification of collagen content (F; Combined n = 14 (*Ahr*$^{fl/fl}$) or n = 12 (*Ahr*$^{fl/fl}$*Villin*$^{Cre+}$), male n = 7 (*Ahr*$^{fl/fl}$) or n = 5 (*Ahr*$^{fl/fl}$*Villin*$^{Cre+}$), female n = 7) and necrotic core content (G; Combined n = 14 (*Ahr*$^{fl/fl}$) or n = 12 (*Ahr*$^{fl/fl}$*Villin*$^{Cre+}$), male n = 7 (*Ahr*$^{fl/fl}$) or n = 5 (*Ahr*$^{fl/fl}$*Villin*$^{Cre+}$), female n = 7). **(H–I)** Representative pictures of MAC2+ stained aortic roots (H; scale = 100 μm) and quantification of MAC2+ cells as a percentage of all DAPI + plaque cells (Combined n = 13 (*Ahr*$^{fl/fl}$) or n = 12 (*Ahr*$^{fl/fl}$*Villin*$^{Cre+}$), male n = 6 (*Ahr*$^{fl/fl}$) or n = 5 (*Ahr*$^{fl/fl}$*Villin*$^{Cre+}$), female n = 7). **(J)** Blood total leukocyte and leukocyte subset counts (Combined n = 12 (*Ahr*$^{fl/fl}$) or n = 11 (*Ahr*$^{fl/fl}$*Villin*$^{Cre+}$), male n = 7 (*Ahr*$^{fl/fl}$) or n = 5 (*Ahr*$^{fl/fl}$*Villin*$^{Cre+}$), female n = 5 (*Ahr*$^{fl/fl}$) or n = 6 (*Ahr*$^{fl/fl}$*Villin*$^{Cre+}$)). Graphs represent mean ± SEM. $^{*}P < 0.05$, $^{**}P < 0.01$.

not observe a clear phenotype in our hepatocyte-specific *Ahr* knockout under the present experimental conditions. This may suggest that the liver effects observed by us [54] and others may potentially not be hepatocyte-driven but rather a consequence of mechanisms that influence the liver. Moreover, because chemical stimulants are used rather than genetic aberrations, the consequences and side effects of the action might differ markedly from those reported in the literature, as observed in our study of hepatocyte-specific *Ahr*-deficient mice. However, to validate and more precisely pinpoint these proposed indirect mechanisms, additional studies are warranted.

In contrast to our findings in the IEC knockout model, in which *Ahr* deficiency conferred protection, several studies report an opposite role for the AhR in lipid metabolism. In mice treated with TCDD, fatty acid and cholesterol synthesis could be inhibited [55]. Similarly, mice treated with B[a]P, another potent AhR activator, showed reduced fat synthesis [56]. In another study by Natividad et al., treating HFD-fed mice with the activator 6-Formylindolo[3,2-b]carbazol (FICZ) reduced plasma cholesterol levels and improved fatty liver symptoms [45]. These

studies report effects opposite to ours and to other studies on AhR involvement in lipid metabolism, but noteworthy, stimulation with external AhR ligand supply inevitably also targets AhR signalling in other cell types, e.g. immune cells, and effects cannot always be assigned to specific organs and/or cell types that may secondarily affect lipid metabolism. Thus, the AhR's role in lipid metabolism may be context-specific and, most likely, ligand-specific. However, it remains to be elucidated which activators primarily act on AhR in IECs in our model.

We discovered that the absence of *Ahr* in intestinal epithelial cells of male mice resulted in decreased expression of *Plpp2, Acot1, Hsd17b13, Srebf1,* and *Cd36* in duodenal tissue. While *Cd36* has already been reported as a downstream target of AhR activation [57], the downregulation of the other genes has not yet been fully described in the context of AhR pathways. However, the prominence of some of these genes in lipid metabolism is already well defined. In humans, HSD17B13 has been strongly associated with MASLD progression [58]. A knock-out of *Acot1* in mice has been reported to protect from HFD-induced obesity [59]. *Srebf1* has been shown to contribute to liver diseases, such as MAFLD, by impacting lipid metabolism [60]; similarly, *Cd36,* as a lipid uptake receptor, is known to be involved in lipid-related diseases, such as obesity [61]; a downregulation of *Plpp2* has been described as protective in the context of diabetes-induced steatosis and inflammation [62]. These results indicate that intestinal epithelial cell-AhR affects the transcription of a variety of genes, many of which are highly relevant to lipid-driven diseases.

In a previous study, we showed that a whole-body knock-out of *Ahr* also leads to reduced lipid accumulation and, thereby, reduced plaque development in mice on a high-fat diet. Interestingly, although the whole-body knockout showed similar effects in both sexes, this study revealed that intestinal epithelial *Ahr* is involved only in male lipid metabolism, suggesting a sex-dependent role of the AhR in lipid metabolism that may differ across cell types [54]. Additionally, the notion that intestinal cholesterol levels remain unchanged while systemic levels decrease in IEC-specific *Ahr*-deficient mice warrants further investigation into potential additional pathways or cellular sources of AhR that contribute to the lipid metabolism phenotype. In this study, male PCSK9-overexpressing $Ahr^{fl/fl}$ $Villin^{Cre+}$ mice exhibited smaller atherosclerotic plaques after a 12-week HFD and contained slightly, but not significantly, more macrophages, indicating a key role of AhR expression in IECs for the development of atherosclerosis. These effects seemed to be driven by different mechanisms in male and female mice. While male atherosclerosis improvement in IEC-specific *Ahr*-deficient mice appeared to be driven by altered lipid metabolism, this was not the case in female mice. Despite the absence of changes in intestinal or systemic lipid metabolism in female mice, AhR knockout in IECs still reduced atherosclerosis development. In these mice, we observed differences in blood leukocyte counts that may have hindered atherosclerotic plaque development in female mice. Similarly, even though not always consistent, observations of reduced leukocyte counts in *Ahr*-deficiency have been reported earlier: While one *Ahr*-deficient mouse strain exhibited reduced T- and B-cell counts in several organs, two other strains generated simultaneously showed no effects. These alterations were explained by differences in the microbiome between the strains [63]. Since an HFD can alter the intestinal microbiome, and this effect appears to be sex-dependent, the observed sex differences in our study may also result from differences in the microbiome between males and females [64]. It is generally acknowledged that female mice exhibit higher levels of inflammatory mediators and cytokines, with a predominance of leukocytosis compared with males [65]. Despite the lack of differences in measured circulating cytokines, it is plausible that other inflammatory mediators are altered, which, in our case, could be the cause for the observed higher leukocyte levels in female mice. It has, for example, already been shown that the AhR mediates cytokine signalling in various contexts. In the intestine, interleukin 22 (IL-22), a key regulator of intestinal homeostasis, can be directly be regulated by the AhR in ILC3s [66]. Moreover, diverse studies point out an AhR-mediated cytokine release of interleukin 6 (IL-6), interleukin 10 (IL-10) and interleukin 33 (IL-33), which seems to be guided via AhR-STAT interaction [67]. These processes, however, have mainly been observed in immune cells [67], which aligns with the lack of effects on cytokine levels in our study, as the *Ahr* deficiency in our model affected epithelial cells rather than immune cells. Nevertheless, secondary downstream effects on, for instance, intestinal immune cells cannot be ruled out and warrant further investigation.

Additionally, a few studies similar to ours observed a sexually dimorphic pattern in downstream expression following AhR activation. For instance, TCDD activation was shown to lead to a sex-dependent hepatic transcriptome [68], and mice lacking *Ahr* in specific immune cells exhibited sex-dependent differences in gene expression, concomitant with a sex-dependent switch in the gut microbiome [69]. It has been reported that sex hormones can influence certain aspects of lipid metabolism. In the liver, for instance, estrogen has been shown to interfere with triglyceride metabolism, more specifically, triglyceride accumulation [70]. Concerning intestinal lipid metabolism, already in 1998, it was reported that high doses of estrogen increase intestinal cholesterol absorption, leading to a higher risk of gallstones due to increased bile acid production [71,72]. More recently, it has been reported that estradiol and progesterone may interfere with the intestinal absorption and lymphatic transport of dietary lipids by reducing chylomicron transport and increasing apolipoprotein A-1 synthesis, thereby affecting high-density lipoprotein particle levels [73]. These results also align with findings in this study that estrogen treatment of IECs attenuates the effects of *Ahr* deficiency on lipid-related gene expression. As mentioned before, HFD changes the intestinal microbiome in a sex-dimorphic manner, which indirectly also impacts parts of intestinal lipid conversion [74]. These data suggest that sex hormones affect intestinal lipid metabolism, although further studies are warranted to validate this suggestion.

These results, combined with our data, suggest that AhR activation has distinct downstream mechanisms that are sex-dependent. The precise mechanism underlying the female-specific effect on leukocytes remains unclear, and further research is needed to elucidate the impact of intestinal AhR on blood leukocyte levels. For example, depletion of leukocytes or leukocyte subsets could be performed in combination with the IEC-specific *Ahr*-deficient model to determine the extent to which leukocytes contribute to the observed atherosclerosis effects in females.

Overall, this study identified the AhR as a novel mediator of intestinal lipid metabolism in males, regulating diverse intestinal lipid pathways. While the hepatocyte-specific AhR does not appear to play a major role in lipid metabolism or systemic hyperlipidaemia under the current experimental conditions and has no effect on atherosclerosis in our model, AhR in IECs of male mice on an HFD appears to significantly affect local and systemic lipid metabolism. This knowledge provides a basis for novel lipid-lowering treatment options via intestinal epithelial AhR activity; however, caution is warranted given observed sex dimorphism and described context specificity.

Data sharing

Data is deposited in publicly available databases as described in the method section or available upon reasonable request.

Funding

Corona-Foundation (S199/10084/2021), Deutsche-Forschungsgemeinschaft (SFB-TRR219/Project-ID:322900939 and INST 222/1598-1 FUGG; Projekt: 566187929; E.P.C.v.d.V.), Ernst-und-Berta-Grimmke-Stiftung (9/22; J.M.), German-Federal-Ministry-of-Education-and-Research (01KD2435; S.D.). C.O received funding from the German Research Foundation (project number OH 282/1-2 within FOR2599, SZ 429/1-1 and OH 282/3-1, CRC1371/2 project number 395357507 – P07 and SFB/TRR 355/1 project number: 490846870 - A05).

Conflict of interest

None.

Acknowledgements

This work was supported by the Flow Cytometry Facility and Genomics Facility, core facilities of the Interdisciplinary Center for Clinical Research (IZKF) Aachen within the Faculty of Medicine at RWTH Aachen University.

Appendix A. Supplementary data

Supplementary data to this article can be found online at https://doi.org/10.1016/j.atherosclerosis.2026.121857.

References

[1] Fan J, Watanabe T. Atherosclerosis: known and unknown. Pathol Int 2022;72(3):151–60.
[2] Lechner K, von Schacky C, McKenzie AL, Worm N, Nixdorff U, Lechner B, et al. Lifestyle factors and high-risk atherosclerosis: pathways and mechanisms beyond traditional risk factors. Eur J Prev Cardiol 2020;27(4):394–406.
[3] Rajendran P, Rengarajan T, Thangavel J, Nishigaki Y, Sakthisekaran D, Sethi G, et al. The vascular endothelium and human diseases. Int J Biol Sci 2013;9(10):1057–69.
[4] Favero G, Paganelli C, Buffoli B, Rodella LF, Rezzani R. Endothelium and its alterations in cardiovascular diseases: life style intervention. Biomed Res Int 2014;2014:801896.
[5] Pirillo A, Norata GD, Catapano AL. LOX-1, OxLDL, and atherosclerosis. Mediat Inflamm 2013;2013:152786.
[6] Falk E. Pathogenesis of atherosclerosis. J Am Coll Cardiol 2006;47(8 Suppl):C7–12.
[7] Bobryshev YV. Monocyte recruitment and foam cell formation in atherosclerosis. Micron 2006;37(3):208–22.
[8] Zhang S, Hong F, Ma C, Yang S. Hepatic lipid metabolism disorder and atherosclerosis. Endocr Metab Immune Disord Drug Targets 2022;22(6):590–600.
[9] Huchzermeier R, de Jong RJ, Rakateli L, Bonnin-Marquez A, Maas SL, Maassen-Pottgens C, et al. Whole-body knockout of the AhR (Aryl hydrocarbon receptor) ameliorates atherosclerosis due to altered lipid metabolism-brief report. Arterioscler Thromb Vasc Biol 2026;46(3):e323673.
[10] Maier AM, Huth K, Alessandrini F, Schnautz B, Arifovic A, Riols F, et al. The aryl hydrocarbon receptor regulates lipid mediator production in alveolar macrophages. Front Immunol 2023;14:1157373.
[11] Rakateli L, Huchzermeier R, van der Vorst EPC. AhR, PXR and CAR: from xenobiotic receptors to metabolic sensors. Cells 2023;12(23).
[12] Rothhammer V, Quintana FJ. The aryl hydrocarbon receptor: an environmental sensor integrating immune responses in health and disease. Nat Rev Immunol 2019;19(3):184–97.
[13] Denison MS, Nagy SR. Activation of the aryl hydrocarbon receptor by structurally diverse exogenous and endogenous chemicals. Annu Rev Pharmacol Toxicol 2003;43:309–34.
[14] McMillan BJ, Bradfield CA. The aryl hydrocarbon receptor is activated by modified low-density lipoprotein. Proc Natl Acad Sci USA 2007;104(4):1412–7.
[15] Carambia A, Schuran FA. The aryl hydrocarbon receptor in liver inflammation. Semin Immunopathol 2021;43(4):563–75.
[16] Krishnan S, Ding Y, Saedi N, Choi M, Sridharan GV, Sherr DH, et al. Gut microbiota-derived tryptophan metabolites modulate inflammatory response in hepatocytes and macrophages. Cell Rep 2018;23(4):1099–111.
[17] Ko CW, Qu J, Black DD, Tso P. Regulation of intestinal lipid metabolism: current concepts and relevance to disease. Nat Rev Gastroenterol Hepatol 2020;17(3):169–83.
[18] Huchzermeier R, van der Vorst EPC. Aryl hydrocarbon receptor (AHR) and nuclear factor erythroid-derived 2-like 2 (NRF2): an important crosstalk in the gut-liver axis. Biochem Pharmacol 2025;233:116785.
[19] Stockinger B, Shah K, Wincent E. AHR in the intestinal microenvironment: safeguarding barrier function. Nat Rev Gastroenterol Hepatol 2021;18(8):559–70.
[20] Qian M, Liu J, Zhao D, Cai P, Pan C, Jia W, et al. Aryl hydrocarbon receptor deficiency in intestinal epithelial cells aggravates alcohol-related liver disease. Cell Mol Gastroenterol Hepatol 2022;13(1):233–56.
[21] Bankhead P, Loughrey MB, Fernandez JA, Dombrowski Y, McArt DG, Dunne PD, et al. QuPath: open source software for digital pathology image analysis. Sci Rep 2017;7(1):16878.
[22] Bray NL, Pimentel H, Melsted P, Pachter L. Near-optimal probabilistic RNA-seq quantification. Nat Biotechnol 2016;34(5):525–7.
[23] Soneson C, Love MI, Robinson MD. Differential analyses for RNA-seq: transcript-level estimates improve gene-level inferences. F1000Res 2015;4:1521.
[24] Love MI, Huber W, Anders S. Moderated estimation of fold change and dispersion for RNA-seq data with DESeq2. Genome Biol 2014;15(12):550.
[25] Liberzon A, Birger C, Thorvaldsdottir H, Ghandi M, Mesirov JP, Tamayo P. The molecular signatures database (MSigDB) hallmark gene set collection. Cell Syst 2015;1(6):417–25.
[26] Yu G. Thirteen years of clusterProfiler. Innovation (Camb) 2024;5(6):100722.
[27] Wu T, Hu E, Xu S, Chen M, Guo P, Dai Z, et al. clusterProfiler 4.0: a universal enrichment tool for interpreting omics data. Innovation (Camb) 2021;2(3):100141.
[28] Xu S, Hu E, Cai Y, Xie Z, Luo X, Zhan L, et al. Using clusterProfiler to characterize multiomics data. Nat Protoc 2024;19(11):3292–320.
[29] Stacklies W, Redestig H, Scholz M, Walther D, Selbig J. pcaMethods–a bioconductor package providing PCA methods for incomplete data. Bioinformatics 2007;23(9):1164–7.
[30] Chirumamilla CS, Fazil M, Perez-Novo C, Rangarajan S, de Wijn R, Ramireddy P, et al. Profiling activity of cellular kinases in migrating T-Cells. Methods Mol Biol 2019;1930:99–113.
[31] Yu G, Wang LG, Han Y, He QY. clusterProfiler: an R package for comparing biological themes among gene clusters. OMICS 2012;16(5):284–7.
[32] Team RC. R: A language and environment for statistical computing. R Foundation for Statistical Computing, Vienna, Austria. . URL https://wwwR-projectorg/.2013.
[33] Wickham H. ggplot2: elegant graphics for data analysis. Springer International Publishing; 2016.
[34] Turei D, Valdeolivas A, Gul L, Palacio-Escat N, Klein M, Ivanova O, et al. Integrated intra- and intercellular signaling knowledge for multicellular omics analysis. Mol Syst Biol 2021;17(3):e9923.
[35] Goel R, Harsha HC, Pandey A, Prasad TS. Human protein reference database and human proteinpedia as resources for phosphoproteome analysis. Mol Biosyst 2012;8(2):453–63.
[36] Hornbeck PV, Zhang B, Murray B, Kornhauser JM, Latham V, Skrzypek E. PhosphoSitePlus, 2014: mutations, PTMs and recalibrations. Nucleic Acids Res 2015;43(Database issue):D512–20.
[37] Diella F, Gould CM, Chica C, Via A, Gibson TJ. Phospho.ELM: a database of phosphorylation sites–update 2008. Nucleic Acids Res 2008;36(Database issue):D240–4.
[38] Milacic M, Beavers D, Conley P, Gong C, Gillespie M, Griss J, et al. The reactome pathway knowledgebase 2024. Nucleic Acids Res 2024;52(D1):D672–8.
[39] Damle NP, Kohn M. The human DEPhOsphorylation database DEPOD: 2019 update. Database (Oxford) 2019:2019.
[40] Schwarz N, Leube RE, Dusterhoft S. Comprehensive in silico analyses of keratin heterodimerisation. Eur J Cell Biol 2025;104(4):151513.
[41] Oughtred R, Rust J, Chang C, Breitkreutz BJ, Stark C, Willems A, et al. The BioGRID database: a comprehensive biomedical resource of curated protein, genetic, and chemical interactions. Protein Sci 2021;30(1):187–200.
[42] Jumper J, Evans R, Pritzel A, Green T, Figurnov M, Ronneberger O, et al. Highly accurate protein structure prediction with AlphaFold. Nature 2021;596(7873):583–9.
[43] Mirdita M, Schutze K, Moriwaki Y, Heo L, Ovchinnikov S, Steinegger M. ColabFold: making protein folding accessible to all. Nat Methods 2022;19(6):679–82.
[44] Varga JK, Ovchinnikov S, Schueler-Furman O. actifpTM: a refined confidence metric of AlphaFold2 predictions involving flexible regions. Bioinformatics 2025;41(3).
[45] Natividad JM, Agus A, Planchais J, Lamas B, Jarry AC, Martin R, et al. Impaired aryl hydrocarbon receptor ligand production by the gut microbiota is a key factor in metabolic syndrome. Cell Metab 2018;28(5):737–749 e4.
[46] Sato T, Vries RG, Snippert HJ, van de Wetering M, Barker N, Stange DE, et al. Single Lgr5 stem cells build crypt-villus structures in vitro without a mesenchymal niche. Nature 2009;459(7244):262–5.
[47] Zheng W, Liu M, Lv X, He C, Yin J, Ma J. AhR governs lipid metabolism: the role of gut microbiota. Front Microbiol 2025;16:1442282.
[48] Huang B, Bao J, Cao YR, Gao HF, Jin Y. Cytochrome P450 1A1 (CYP1A1) catalyzes lipid peroxidation of oleic acid-induced HepG2 cells. Biochemistry (Mosc) 2018;83(5):595–602.
[49] Huang T, Song J, Gao J, Cheng J, Xie H, Zhang L, et al. Adipocyte-derived kynurenine promotes obesity and insulin resistance by activating the AhR/STAT3/IL-6 signaling. Nat Commun 2022;13(1):3489.
[50] Moyer BJ, Rojas IY, Kerley-Hamilton JS, Nemani KV, Trask HW, Ringelberg CS, et al. Obesity and fatty liver are prevented by inhibition of the aryl hydrocarbon receptor in both female and male mice. Nutr Res 2017;44:38–50.
[51] Zhang X, Jin M, Chu Y, Liu F, Qu H, Chen C. STK32C activated IL-6/JAK2/STAT3 signaling and promoted tumor angiogenesis. Br J Cancer 2025;134:60–71.
[52] Xu CX, Wang C, Zhang ZM, Jaeger CD, Krager SL, Bottum KM, et al. Aryl hydrocarbon receptor deficiency protects mice from diet-induced adiposity and metabolic disorders through increased energy expenditure. Int J Obes 2015;39(8):1300–9.
[53] Podechard N, Le Ferrec E, Rebillard A, Fardel O, Lecureur V. NPC1 repression contributes to lipid accumulation in human macrophages exposed to environmental aryl hydrocarbons. Cardiovasc Res 2009;82(2):361–70.
[54] Huchzermeier RdJ, R,J. Rakateli, L. Bonnin-Marquez, A. Maas, S, L. Maassen-Pöttgens, C. Abschlag, K. Jin, H. Geiselhöringer, A. Triantafyllidou, V. Santovito, D. Jankowski, J. Biessen, E,A,L. Ohnmacht, C van der Vorst, E.P.C. Whole-body knock-out of the aryl hydrocarbon receptor (AhR) ameliorates atherosclerosis due to altered lipid metabolism. ATVB.
[55] Lakshman MR, Campbell BS, Chirtel SJ, Ekarohita N. Effects of 2,3,7,8-tetrachlorodibenzo-p-dioxin (TCDD) on de novo fatty acid and cholesterol synthesis in the rat. Lipids 1988;23(9):904–6.
[56] Lou W, Zhang MD, Chen Q, Bai TY, Hu YX, Gao F, et al. Molecular mechanism of benzo [a] pyrene regulating lipid metabolism via aryl hydrocarbon receptor. Lipids Health Dis 2022;21(1):13.
[57] Lee JH, Wada T, Febbraio M, He J, Matsubara T, Lee MJ, et al. A novel role for the dioxin receptor in fatty acid metabolism and hepatic steatosis. Gastroenterology 2010;139(2):653–63.

[58] Zhang HB, Su W, Xu H, Zhang XY, Guan YF. HSD17B13: a potential therapeutic target for NAFLD. Front Mol Biosci 2021;8:824776.
[59] Heden TD, Franklin MP, Dailey C, Mashek MT, Chen C, Mashek DG. ACOT1 deficiency attenuates high-fat diet-induced fat mass gain by increasing energy expenditure. JCI Insight 2023;8(18).
[60] Li Z, Jin Y, Zhao H, Gu Y, Zhang Y, Cheng S, et al. Aurantio-obtusin regulates gut microbiota and serum metabolism to alleviate high-fat diet-induced obesity-associated non-alcoholic fatty liver disease in mice. Phytother Res 2025;39(5):1946–65.
[61] Love-Gregory L, Abumrad NA. CD36 genetics and the metabolic complications of obesity. Curr Opin Clin Nutr Metab Care 2011;14(6):527–34.
[62] Choi RY, Ham JR, Lee HI, Cho HW, Choi MS, Park SK, et al. Scopoletin supplementation ameliorates steatosis and inflammation in diabetic mice. Phytother Res 2017;31(11):1795–804.
[63] Stockinger B, Di Meglio P, Gialitakis M, Duarte JH. The aryl hydrocarbon receptor: multitasking in the immune system. Annu Rev Immunol 2014;32:403–32.
[64] Hases L, Stepanauskaite L, Birgersson M, Brusselaers N, Schuppe-Koistinen I, Archer A, et al. High-fat diet and estrogen modulate the gut microbiota in a sex-dependent manner in mice. Commun Biol 2023;6(1):20.
[65] Purdy JC, Shatzel JJ. The hematologic consequences of obesity. Eur J Haematol 2021;106(3):306–19.
[66] Li YY, Wang XJ, Su YL, Wang Q, Huang SW, Pan ZF, et al. Baicalein ameliorates ulcerative colitis by improving intestinal epithelial barrier via AhR/IL-22 pathway in ILC3s. Acta Pharmacol Sin 2022;43(6):1495–507.
[67] Sondermann NC, Fassbender S, Hartung F, Hatala AM, Rolfes KM, Vogel CFA, et al. Functions of the aryl hydrocarbon receptor (AHR) beyond the canonical AHR/ARNT signaling pathway. Biochem Pharmacol 2023;208:115371.
[68] Lee J, Prokopec SD, Watson JD, Sun RX, Pohjanvirta R, Boutros PC. Male and female mice show significant differences in hepatic transcriptomic response to 2,3,7,8-tetrachlorodibenzo-p-dioxin. BMC Genom 2015;16(1):625.
[69] Mitchell C, Staley S, Williams MC, Saxena A, Bogdon R, Roark K, et al. Regulation of Bacteroides acidifaciens by the aryl hydrocarbon receptor in IL-22-producing immune cells has sex-dependent consequential impact on colitis. Front Immunol 2024;15:1444045.
[70] Palmisano BT, Zhu L, Stafford JM. Role of estrogens in the regulation of liver lipid metabolism. Adv Exp Med Biol 2017;1043:227–56.
[71] Henriksson P, Einarsson K, Eriksson A, Kelter U, Angelin B. Estrogen-induced gallstone formation in males. Relation to changes in serum and biliary lipids during hormonal treatment of prostatic carcinoma. J Clin Investig 1989;84(3):811–6.
[72] Uhler ML, Marks JW, Voigt BJ, Judd HL. Comparison of the impact of transdermal versus oral estrogens on biliary markers of gallstone formation in postmenopausal women. J Clin Endocrinol Metab 1998;83(2):410–4.
[73] Liu M, Shen L, Yang Q, Nauli AM, Bingamon M, Wang DQ, et al. Sexual dimorphism in intestinal absorption and lymphatic transport of dietary lipids. J Physiol 2021;599(22):5015–30.
[74] Brettle H, Tran V, Drummond GR, Franks AE, Petrovski S, Vinh A, et al. Sex hormones, intestinal inflammation, and the gut microbiome: major influencers of the sexual dimorphisms in obesity. Front Immunol 2022;13:971048.